Evaluation of the Electronic and Local Structure of Mn in Proton-Conducting Oxide, Ca(Zr,Mn)O$_{3-\delta}$, to Elucidate a Direct Hydrogen-Dissolution Reaction

Masatsugu Oishi,[*,†] Takashi Nakamura,[‡] Iwao Watanabe,[§] Takashi Yamamoto, [†] Takuya Doi, [†]

Toshiaki Ina, [∥] Kiyofumi Nitta, [∥] Koji Amezawa,[‡] Yuji Okuyama[⊥]

[†]*Graduate School of Technology, Industrial and Social Sciences, Tokushima University, 2-1*

Minami Josanjima-cho, Tokushima, 770-8506, Japan

[‡]*Institute of Multidisciplinary Research for Advanced Materials, Tohoku University, 2-1-1*

Katahira, Aoba-ku, Sendai, Miyagi   980-8577, Japan

[§]*SR Center, Ritsumeikan University, 1‑1‑1 Nojihigashi, Kusatsu, Shiga 525-8577, Japan*

[∥]*Japan Synchrotron Radiation Research Institute (JASRI), 1‑1‑1 Kouto, Sayo-cho, Sayo-gun,*

Hyogo 679‑5198

[⊥]*Faculty of Engineering, University of Miyazaki, 1-1 Gakuen Kibanadainishi, Miyazaki 889-*

2192, Japan.

[*]**Corresponding author**: Masatsugu Oishi

Address: 2-1 Minami Josanjima-cho, Tokushima 770-8506, Japan

Phone: +81-88-656-7367

E-mail: ooishi.masatsugu@tokushima-u.ac.jp

ABSTRACT

The protonation mechanism in Mn-doped $CaZrO_3$ (CZM), which involves a direct hydrogen dissolution from the surrounding H_2 gas, was investigated by thermogravimetry (TG) and X-ray absorption spectroscopy (XAS). The TG results implied the formation of oxygen vacancies in a H_2 atmosphere. The Mn K-edge XAS spectra indicated a reduction of the Mn ions and local structure variations around the Mn ion, but the Zr K-edge spectra were independent of the surrounding atmosphere. The amount of oxygen vacancies was smaller with respect to the reduction of the Mn ions, suggesting direct dissolution of hydrogen. Unlike many typical perovskite-type proton conductors, protonation by direct dissolution of hydrogen and not hydration was the predominant reaction in Mn-doped $CaZrO_3$. Our experimental results demonstrated that the hydration reaction was suppressed because the oxygen vacancy was stable in the distorted ZrO_6 symmetry in the $CaZrO_3$ crystal host, whereas protonation proceeded by the direct dissolution of hydrogen stabilizing near the Mn ions in the interstitial sites at the distorted MnO_6 octahedron symmetry. The experimental results showed that the structural configurations around dopants play important roles in the stabilization of protons in perovskite-type CZM materials. We demonstrated a new group of proton conductors that can overcome issues with conventional proton conductors by utilizing the direct hydrogen dissolution reaction.

1. INTRODUCTION

A solid oxide fuel cell (SOFC) uses an oxide electrolyte in which oxygen ions diffuse. It operates at a high temperature (about 1073-1273 K), which enables high-efficiency and high-power generation. Practical uses have already been reported.[1-4] However, the high operating temperature has become a hurdle for full-scale dissemination. A perovskite-type proton conducting oxide hold promise as an electrolyte in intermediate temperature SOFCs (IT-SOFC), or it is also referred as proton ceramic fuel cell (PCFC), because it exhibits a high diffusion of protons below 873 K under a water vapor atmosphere.[5-12] Perovskite-type oxides of acceptor-doped $BaCeO_3$ and $BaZrO_3$ show high proton conductivities, and they have been mainly examined as electrolytes for PCFCs.[13-22] Generally, $BaCeO_3$ materials show higher proton conductivity compared to that of $BaZrO_3$ materials. However, the $BaCeO_3$ materials are unstable against a CO_2 or H_2O atmosphere.[6,19] Hence, a chemically stable proton conductive oxide with an excellent mechanical strength is necessary for practical PCFC applications. The perovskite-type oxide of $CaZrO_3$ is chemically stable and has an excellent mechanical strength,[23-25] but its proton conductivity is unfortunately poor due to the low solubility of protons.[26,27]

Protonation in the acceptor-doped $CaZrO_3$ such as In-doped $CaZrO_3$ has been explained using the Kröger–Vink notation[28] as follows:

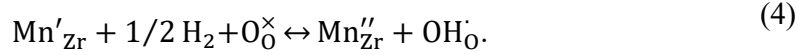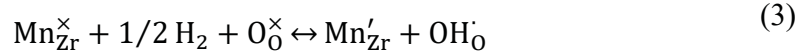Doped In^{3+} ions substitute for Zr^{4+} ions, resulting in the formation of oxygen vacancies as

$$In_2O_3 \rightarrow 2In'_{Zr} + V_O^{\cdot\cdot} + 3O_O^\times \quad (1)$$
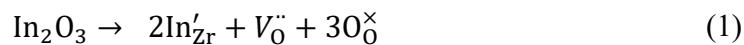
Protonation via the hydration reaction through an oxygen ion vacancy in a wet condition as

$$H_2O + O_O^\times + V_O^{\cdot\cdot} \rightleftarrows 2OH_O^{\cdot} \quad (2)$$

The protons in In-doped $CaZrO_3$ only dissolve about several% of the oxygen ion vacancy concentration.[26] Hence, protons are not saturated with respect to the amount of the oxygen vacancies. On the other hand, protons in Y-doped $BaZrO_3$ are substantially saturated in the oxygen vacancies.[5,6,29] The difference in the hydration reaction between $CaZrO_3$ and $BaZrO_3$ may be explained by the basicity of the oxygen lattice as suggested by Kreuer.[6]

$BaZrO_3$ shows a symmetric cubic structure and the ZrO_6 octahedra are connected in an ordered symmetry, while $CaZrO_3$ is an orthorhombic structure consisting of ZrO_6 octahedra with corner sharing and a distorted symmetry. Takahashi et al.[30] reported the density functional theory (DFT) computation analysis of acceptor-doped $BaZrO_3$, and evaluated the hydration reaction for different dopant elements. They suggested that the hydration reaction is affected by the local structural configuration as well as the formation of oxygen vacancies. Protons in $BaZrO_3$ materials are prone to stabilize away from the distorted configuration. Islam et al.[31] also reported DFT calculation results in $BaZrO_3$ materials. The binding energies of dopants and hydroxyl pairs varied by the different acceptor species, which implied the stability of protons may be related to the basicity as well to the local structure. Therefore, in addition to the lower basicity of Ca based compounds, the low proton dissolution in the $CaZrO_3$ materials may be due to its local structure in which the apex-oxygen connection of ZrO_6 octahedron is highly distorted.

Okuyama et al.[32] reported a redox protonation in a Mn-doped $Ca(Zr_{1-x}Mn_x)O_{3-\delta}$ (CZM) material in which hydrogen directly dissolves in the H_2 atmosphere. The electron spin resonance spectra indicate that the Mn ions are reduced in a H_2 atmosphere. Accordingly, H_2 gas directly dissolves into the crystal to satisfy the electroneutrality of CZM. The hydrogen dissolution reaction is described by the following equations

$$Mn_{Zr}^{\times} + 1/2\,H_2 + O_O^{\times} \leftrightarrow Mn'_{Zr} + OH_O^{\cdot} \qquad (3)$$

$$Mn'_{Zr} + 1/2\,H_2 + O_O^{\times} \leftrightarrow Mn''_{Zr} + OH_O^{\cdot}. \qquad (4)$$

Generally, the formation of oxygen vacancies compensates for the reduced valences of the acceptor ions,[33,34] and the hydration reaction proceeds in wet gas conditions. Therefore, hydration reaction expressed in equation (2) depends only on H_2O activity and independent on the H_2 activity. However, the proton conductivity of CZM depends only on the H_2 activity of the atmosphere, and the proton conductivity increases with the increase in the H_2 activity of the surrounding atmosphere. These dependences cannot be explained by the conventional hydration reaction. Based on the electromotive force (EMF) of a gas concentration cell using CZM as the electrolyte, proton is the predominant carrier in the H_2 atmosphere. EMF of the water vapor concentration cell at a constant H_2 activity is not observed. Hence, the oxide ion conductivity is very small compared to the proton conductivity. In addition, the IR absorption spectra show O-H vibrations only in a H_2 atmosphere. Therefore, the protonation reaction in CZM is explained by the hydrogen dissolution using the redox reaction of the Mn ions expressed in equations (3) and (4) but not the hydration reaction expressed in equation (2).

Direct dissolution of hydrogen by the redox reaction of transition metals was reported in Ni- and Co-doped sapphire a-Al_2O_3 by Günthard $et\ al.$ in 1966.[35] Ni^{3+} and Co^{3+} in Al site are reduced to Ni^{2+} and Co^{2+} in H_2 atmospheres, and proton dissolves to charge compensate the valence changes of the transition metals.[36,37] Also, Matsumoto $et\ al.$ [38] reported the redox protonation reaction proceeding in Mn-doped $SrZrO_3$. Conventionally, rare-earth elements such as Y- and In- doped in $AZrO_3$ (A=Ca, Sr, Ba) materials are charge compensated by the formation of oxygen vacancies. Then, the protons dissolve by the hydration reaction via oxygen vacancies in the H_2O containing atmospheres. This reaction is essentially dependent on the oxygen vacancy

concentration. In addition, the hydration reaction is determined both by the diffusion of protons and the oxide ions.[6] Consequently, lowering the operation temperature is difficult. In contrast, for 3d transition metal-doped perovskite-type oxides such as Mn-doped $SrZrO_3$ and $CaZrO_3$ materials, hydrogen directly dissolves into the crystal to compensate for the charge reduction of Mn ions in a H_2 atmosphere. Ideally, it depends only on the H_2 activity and hole concentrations, and it is independent on the diffusion of protons and the oxide. Hence, it has a potential to be used at the lower-temperature operations for PCFCs.

The redox protonation in Ni- and Co- doped a-Al_2O_3 was explained solely by the dissolution of hydrogen because the other defects such as the oxygen vacancy are unlikely formed in H_2 atmosphere. However, in the case of $AZrO_3$ materials, oxygen vacancy also formed in H_2 atmosphere, and hydration reaction proceeds in the H_2O containing atmosphere. Hence, the redox protonation in Mn-doped $CaZrO_3$[32] and $SrZrO_3$[38] exists in competition with the conventional hydration reaction. We presume that both the hydration reaction and redox protonation reaction are effected by the variations of the crystal structure of the materials. To understand the hydrogen dissolution reaction occurring in CZM, herein X-ray absorption fine structure (XAFS) analysis is applied to evaluate the electronic and local structures of the Mn and Zr ions. The X-ray absorption near edge structure (XANES) was analyzed to evaluate the valence changes of the Mn and Zr ions. Furthermore, the extended X-ray absorption fine structure (EXAFS) was analyzed to assess the local structure variation caused by the valence change of the Mn ions and the dissolution of protons. In addition, we evaluated the evolution and dissolution of oxygen and hydrogen from thermogravimetry measurements. The relationship between the proton dissolution and local structural variations is discussed.

2. EXPERIMENTAL SECTION

2.1 Sample Preparation and XAFS Measurement

Samples of $Ca(Zr_{1-x}Mn_x)O_{3-\delta}$ ($x=0.015$, 0.005) were prepared by a solid-state reaction method.[32] Reagent-grade $CaCO_3$ (High Purity Chemicals, 99.99%), ZrO_2 (Tosoh, 99.9%), and $MnCO_3$ (Aldrich, 99.9%) powders were weighed, mixed in a zirconia mortar with ethanol, and calcinated at 1573 K for 10 h in air. The calcinated powders were ground in ethanol by a ball mill for 1 h. The powders were pressed into pellets by a cold isostatic press at 250 MPa and sintered at 1773 K for 10 h in air.

The $Ca(Zr_{1-x}Mn_x)O_{3-\delta}$ ($x= 0.05$) samples were prepared by a chemical solution method. Reagent-grade $Ca(NO_3)_2 \cdot 5H_2O$ (Wako, 99.9%), $ZrO(NO_3)_2 \cdot 2H_2O$ (Kanto Kagaku, 99.9%), and $Mn(NO_3)_2 \cdot 6H_2O$ (Wako, 99.9%) were weighed and added into an aqueous solution sequentially with continuous stirring at 423 K. EDTA (Dojindo, 99%) and citric acid (Wako, 98%) were then added as chelating agents with a 1:1:1 molar ratio of the total metal ions to EDTA and citric acid. An ammonium hydroxide solution (Kishida Kagaku, 28.0% NH_3 in H_2O) was added to promote the dissolution of EDTA and to adjust the pH between 8 and 9. The solution was then heated under stirring to evaporate water until it changed into a viscous gel. The gel was then heat-treated at 623 K to obtain a solid precursor and calcined at 1173 K for 10 h in air. Finally, the calcined powder was sintering at 1673 K for 10 h in air.

The X-ray diffraction (XRD) profiles of all samples gave a well-defined perovskite pattern of $CaZrO_3$. The powders were heat treated under different hydrogen / oxygen partial pressures at 1073 K for 20 h for $Ca(Zr_{1-x}Mn_x)O_{3-\delta}$ ($x=0.05$), and 12 h for $Ca(Zr_{1-x}Mn_x)O_{3-\delta}$ ($x=0.015$ and 0.005). The crystal structure of the powders annealed in these atmospheres were measured using X-ray diffraction (XRD, Miniflex600, Rigaku) with Cu Kα radiation at room temperature. Rietveld

refinement was carried out, and the lattice parameters for each sample were determined. Thermogravimetry (TG) was measured using TG (STA 449 F1 Jupiter, NETZSCH) under O_2 and H_2 atmospheres at the constant temperature of 1073 K. The water vapor of the gas was controlled by introducing the gas through a water bubbler set in the temperature controlled water bath. The water bath was set at 290 K. It corresponds to a water vapor pressure $P(H_2O)$ of 0.019 bar.

The XAS measurements of the Mn and Zr K-edges were performed using beamline BL01B1 at SPring-8 (Hyogo, Japan).[39] The Zr K-edge spectra were measured in the transmission mode using Si (311) double-crystal monochromator. The energy scale was calibrated using a Zr foil. The intensities of incident and transmitted X-rays were simultaneously monitored by ionization chambers. The Mn K-edge spectra were measured in the fluorescence mode using Si (111) double-crystal monochromator. The energy scale was calibrated using a Cu foil. The intensities of incident and transmitted X-rays were simultaneously monitored by ionization chambers and 19-element Ge solid–state detector, respectively. The XAFS spectra were analyzed by the IFEFFIT program code using ATHENA and ARTEMIS. [40]

3. RESULTS

3.1 X-ray Diffraction Measurements

The XRD profiles for $Ca(Zr_{1-x}Mn_x)O_{3-\delta}$ (x=0.005, 0.015 and 0.05) annealed in various O_2 and H_2 atmospheres are shown in Fig. 1(a), (b) and (c), respectively. The XRD peaks coincided with that of pure $CaZrO_3$, implying a single phase of Mn-doped $CaZrO_3$ materials. The observed peaks were assigned to the orthorhombic phase (space group: *Pnma*). The XRD patterns were fitted with Rietveld analysis using software of PDXL2 (Rigaku, Japan) which works based on RIETAN-FP.[41] (One of the Rietveld refinement results is shown in Fig. S1). The lattice parameters

are shown in Table.1. The lattice volume decreased with the increasing the Mn content due to the smaller Mn ionic radius compared to the Zr ions, implying the Zr sites are replaced with the Mn ions.

Figure 1(d) plots the lattice volumes as functions of the hydrogen partial pressure $P(H_2)$ and the oxygen partial pressure $P(O_2)$. The lattice parameters were larger for the H_2-annealed samples compared to those for the O_2-annealed samples. This is due to the larger Mn ionic radius for the lower valence states in H_2 atmospheres. The valence changes of the Mn ions are discussed in detail from the XAFS results in Section 3.3. In addition, the color of the CZM powders changed between the O_2 and H_2 atmospheres. The O_2 annealed powders were a dark color, while the H_2 annealed powders showed a pinkish color (Fig. S2). The color difference between the O_2 and H_2 atmospheres implied a change in the electronic structures.

3.2 TG Measurements

At a constant temperature of 1073 K, weight loss was observed after the atmosphere was changed from 0.8%O_2-99.2%Ar gas to 0.8%H_2-99.2%Ar gas in $CaZr_{0.95}Mn_{0.05}O_{3-\delta}$ (Fig.2). In a dry H_2 atmosphere, the evolution of oxygen should cause a decrease in weight, while the dissolution of hydrogen should result in an increase in weight. The decreased weight in 0.8%H_2-99.2%Ar confirmed the formation of oxygen vacancies, but the amount could not be calculated from the results since a certain amount of hydrogen dissolution should increase the weight in a H_2 atmosphere.

Water vapor was introduced to 0.8%H_2-99.2%Ar gas at a water vapor pressure $P(H_2O)$ of 1.9 bar. The weight increased, which implied the dissolution of water by the hydration reaction (Eq.(4)). Finally, the introduction of 0.8%O_2-99.2%Ar wet gas increased the weight, which is

simply explained by the dissolution of oxygen from the surrounding O_2 atmosphere. Details of the concentrations of oxygen vacancies and protons are discussed with the XAFS results in the Discussion.

To validate the electronic and local structures of CZM in the O_2 and H_2 atmospheres, we conducted the XAFS measurements.

3.3 XAFS Measurements

3.3.1 Zr K-edge XANES and EXAFS Spectra

The Zr K-edge XANES spectra of the CZM samples at various O_2 and H_2 annealing atmospheres are shown in Fig.3. The Zr K-edge spectrum was almost unchanged, indicating that the electronic states of the Zr ions are unchanged. The absorption edge of the CZM samples coincided with that of ZrO_2, suggesting the samples have tetravalent (Zr^{4+}) states. Figure 4 shows the Zr K-edge EXAFS oscillations of the samples at various annealing atmospheres. The absorption energy E_0 was selected as the energy of the 1/2 of the normalized absorption jump. Figure 5 shows the amplitudes of Fourier transforms $\chi(R)$ obtained from k^3-weighted EXAFS oscillations. The weighted spectra were Fourier transformed in a k space of 3 to 14 Å^{-1}. The spectra were mostly unchanged, implying that the local structure around the Zr ions was unchanged between the O_2 and H_2 atmospheres.

3.3.2 Mn K-edge XANES Spectra

The Mn K-edge XANES spectra of the CZM samples annealed at various O_2 and H_2 atmospheres are shown in Fig. 6. Included are the spectra for MnO, $LaMnO_3$, and $CaMnO_3$ as references for the Mn^{2+}, Mn^{3+}, and Mn^{4+} states, respectively. CZM had an orthorhombic

perovskite-type structure (space group: *Pnma*). The reference sample of CaMnO$_3$ (Mn^{4+}) had the orthorhombic perovskite-type structure of the *Pnma* space group. The LaMnO$_3$ (Mn^{3+}) had the orthorhombic perovskite-type structure of the *Pbnm* space group, and the MnO$_6$ octahedron is distorted by the Jahn-Teller effect. For the tetravalent ion reference, MnO (Mn^{2+}) of a cubic structure (space group: *Fm-3m*) was used because a material with a similar local structure could not be obtained.

The edge energy of CZM in an O$_2$ atmosphere was similar to that of CaMnO$_3$, suggesting the mean oxidation state of Mn was close to 4+. The edge energy shifted to a lower photon energy in a H$_2$ atmosphere compared to that of an O$_2$ atmosphere, implying that the Mn ions were reduced between 3+ and 2+ in a H$_2$ atmosphere. The edge energy of the O$_2$-annealed samples was independent of the O$_2$ activities, while the edge energy of the H$_2$-annealed samples depended on the H$_2$ activities and the Mn ion concentrations. The edge energy shifted to a lower energy for higher H$_2$ and Mn ion concentrations.

3.3.3 Mn K-edge EXAFS Spectra

Figure 7 shows the Mn K-edge EXAFS oscillations of the CZM samples at various O$_2$ and H$_2$ atmospheres. The EXAFS oscillations were different between the O$_2$ and H$_2$ atmospheres, reflecting changes in the local structures between oxidizing and reducing atmospheres. Figure 8 shows the amplitudes of the Fourier transforms (FT) obtained from EXAFS oscillations. The weighted spectra were Fourier transformed in a *k* space of 3 to 12 Å^{-1}.

To evaluate the EXAFS oscillation and FT spectra, backscattering curved wave amplitude and its phase, and FT amplitude of the single scattering paths of the nearest O, Ca and Zr ions were simulated by the FEFF mode around the Mn ion. The crystal structure of CZM for FEFF

calculation was obtained by the Mn ion replacing the Zr site in the $CaZrO_3$ structure (ICSD 97464) [42]. (See Tables S1 and S2 for details about the crystal structure and Fig.S3 for the simulated spectra.) The first coordination shell represented the Mn-O distances of the MnO_6 octahedron in which the six Mn-O distances were similar. The second coordination shell represented the Mn-Ca distances of the $MnCa_{12}$ hexahedron in which three distinct Mn-Ca distances exist. The third coordination shell corresponded to the Mn-Zr distance of $MnZr_6$ octahedron.

The simulated FT spectra were calculated as an isomorphic substitution of a Mn ion in a Zr site. The simulated FT peak of the third coordination shell corresponding to Mn-Zr was large compared to the experimental FT spectra of CZM. Hence, it suggests that the actual position of the Mn in CZM was different from the original Zr site. For the O_2-annealed CZM samples, the intensity of the first FT peak, which represented the Mn-O distance, was large, while those of the second and third peaks, which represented the Mn-Ca and Mn-Zr distances, were weak. For the H_2-annealed CZM samples, the first FT peak intensity decreased with the increase of H_2 activity. The decrease of FT intensity implied a decrease in the coordination number of oxygen and/or distortion of the MnO_6 octahedron symmetry.

3.3.4 Mn K-edge XAFS Spectra in Dry and Wet Atmospheres

To evaluate the influence of water vapor on the electronic and local structures, we investigated samples annealed in a dry atmosphere. A dry atmosphere was prepared by passing gases through phosphorus (V) oxide (Wako, 98%). The Mn K-edge XAFS spectra of $Ca(Zr_{1-x}Mn_x)O_{3-\delta}$ (x=0.005 and 0.05) were almost the same for the dry and wet atmospheres in the O_2 and H_2 atmospheres (Fig.S4 and Fig.S5). Hence, the electronic states of the Mn ions were independent of the H_2O contents. The FT spectra of the annealed samples in the dry gases also showed that

the first FT peak decreased in the H_2 atmospheres compared to the O_2 atmospheres (Fig. S6). Therefore, the variations of the electronic and local structures in the O_2 and H_2 atmospheres were independent of the H_2O activity. Hence, the electronic and local structure variations between the O_2 and H_2 atmospheres were attributed to both the formation of oxygen vacancies and the redox protonation reaction, but not the hydration reaction.

4. DISCUSSION

The XRD results showed that CZM maintained its space group in both O_2 and H_2 atmospheres. Because the Mn ions replaced the Zr sites, the local structure of the Mn and Zr ions should be the same. However, the XANES spectral shape at the Zr K-edge (Fig. 3) and the Mn K-edge (Fig. 7) differed, suggesting different local structures around the Zr ions and the Mn ions as the XANES spectrum reflects the local structure symmetry. In addition, as already discussed in Section 3.3.3, different FT intensity of the third coordination shell around 3.5 Å (in Fig.8 and Fig.S3) between the experimental spectra and the simulated spectra also suggested the different local structures for the Mn and Zr ions. There is no contradiction in the Mn K-edge XANES spectra and the EXAFS spectra. This is supposedly due to the smaller ionic radius of the Mn ions partially substituted in the larger Zr sites. During the protonation reaction in CZM, the local structure around the Zr ions was nearly unchanged, whereas that of the Mn ions depended on the surrounding atmosphere.

Figure 9 shows the Mn K-edge photon energies at an absorbance of 0.5 for $Ca(Zr_{1-x}Mn_x)O_{3-\delta}$ (x=0.05, 0.015 and 0.005), which is plotted as functions of $P(H_2)$ and $P(O_2)$. Additionally, those of MnO (Mn^{2+}), $LaMnO_3$ (Mn^{3+}), and $CaMnO_3$ (Mn^{4+}) are shown as references for the Mn valence states. In an O_2 atmosphere, the edge energy was between those of Mn^{4+} and Mn^{3+} states but much closer to that of the Mn^{4+} state. The K-edge photon energy shifted to a lower energy in

a higher $P(H_2)$ atmosphere, indicating a reduction of the Mn ions in a reduced atmosphere. For Ca(Zr$_{1-x}$Mn$_x$)O$_{3-\delta}$ (x=0.005 and 0.015), the K-edge photon energies were close to the Mn^{3+} state, while those of Ca(Zr$_{1-x}$Mn$_x$)O$_{3-\delta}$ (x=0.05) further shifted to a lower energy toward the Mn^{2+} state. The average valence states of the Mn ions decreased with the increase in H$_2$ activity. The larger shift of K-edge photon energy for Ca(Zr$_{1-x}$Mn$_x$)O$_{3-\delta}$ (x=0.05) compared to Ca(Zr$_{1-x}$Mn$_x$)O$_{3-\delta}$ (x=0.015 and 0.005) implies a partial deposition of the Mn ions from the crystal host. However, neither Mn metal nor MnO were recognized from the XRD results (Fig.S7). Hence, the amount of the deposited Mn ion is supposedly small, if any.

The Mn-O distances were obtained by fitting the EXAFS spectra. The first coordination shells were fitted in the q space of the reverse FT spectra obtained between a radical range of 1 and 2 Å. The amplitude reduction factor S$_0{}^2$, Debye-Waller factor σ^2, phase shifts ΔE_0, and distances r for the fitting were calculated by the FEFF code based on the structure models of CaZrO$_3$ where Zr was replaced by the Mn ion. The S$_0{}^2$ value was fixed to 0.858, which was determined from the preliminary fitting of MnO powder. The fitted results are shown in Table 2. The Mn-O distances of the CZM samples in the O$_2$ atmospheres differed by the Mn concentrations; the Mn-O distance decreased with the increase in the Mn concentration as shown in Fig. 10.

Considering the Shannon's ionic radius[43] of Zr^{4+} (0.720 Å) and Mn^{4+} (0.530 Å), it is reasonable that Mn-O distance decreased with the increasing the content of smaller Mn^{4+} ions in the Zr^{4+} sites. This reflects the partial replacement of the Mn ions in the Zr sites of CaZrO$_3$. The coordination numbers obtained by the EXAFS fitting were smaller than 6 of MnO$_6$ octahedron coordination. Hence, oxygen vacancies were already formed in the samples prepared in the O$_2$ atmospheres. This assertion is supported by the results of the XANES analysis where the valence states of the Mn ions were lower than Mn^{4+} state in Zr^{4+} sites. Moreover, the coordination numbers

decreased in a H_2 atmosphere, which represented an increase of oxygen vacancies. Per G. Sundell *et al.*[44] calculated interactions of various dopant atoms (Gd, In, Nd, Sc, Y) and oxygen vacancies in $BaZrO_3$ materials, and suggested that the oxygen vacancies are likely to be trapped near the dopant sites in the material. M. S. Islam *et al.*[28] discussed the association between the dopant ion and the protonic defect in $BaZrO_3$. The position of proton shifts towards a neighboring oxygen and dopant ion. The lowest binding energies are for Y and Gd, and the strongest association is for Sc. The longest dopant–proton distances are for the Gd- and Y-dopants, and it mirrors the variation in binding energy. Recently, Takahashi *et al.*.[30] reported the formation energy of oxygen vacancies in $BaZrO_3$ materials. The oxygen vacancies are likely to occupy the acceptor ion coordination sphere rather than that of Zr. For smaller dopants, such as Al-, Ga-, and Sc-doped $BaZrO_3$, protons at the nearest neighbor are favored. Meanwhile, larger dopants, such as Y-, In-, and Lu-doped $BaZrO_3$, preferred the second nearest neighbor site. The dopant and proton incorporation in $CaZrO_3$ was reported by J. D. Gale et al.[45,46] The small lanthanide dopants such as Sc, Yb in $CaZrO_3$ are predicted to substitute on the Zr-site, and oxygen vacancies are formed to charge compensate the trivalent dopants. The proton transfers from one oxygen ion to the next. These DFT calculations suggested that stability of the protonic defects in the perovskite-type oxides are sensitive to the local structure, such as the type of acceptor dopant ion and ion size, in addition to the basicity of the host crystal host.

The decrease in the first FT peak intensity of CZM in a H_2 atmosphere reflected the reduced oxygen around the Mn and distortion of MnO_6 octahedron. The EXAFS spectra for $Ca(Zr_{1-x}Mn_x)O_{3-\delta}$ (x=0.05) in a H_2 atmosphere showed a decrease in the FT intensity and shifted to a longer Mn-O distance in the H_2 atmospheres. The Mn ions were further reduced and the local structure around the Mn ions were distorted compared to $Ca(Zr_{1-x}Mn_x)O_{3-\delta}$ (x=0.005 and 0.015),

implying that multiple coordination paths were formed around the Mn ion. In a H_2 atmosphere, both the dissolution of hydrogen and the formation of oxygen vacancies proceeded to compensate for the charge reduction of the Mn ions. The DFT calculation suggested the variation of local structure around the dopants for the trivalent lanthanide doped perovskite-type oxides. Our results experimentally showed that the variation of local structure around Mn ion in $CaZrO_3$, which varied depending on the dopant concentrations and ionic size of the dopant. In addition, the crystal host of $CaZrO_3$ materials was composed by the apex-oxygen connections of ZrO_6 octahedron. The apex connection was highly distorted in $CaZrO_3$ materials compared to straightly connected ZrO_6 octahedra in the $BaZrO_3$ materials. Therefore, we presumed that the hydration reaction via oxygen vacancy was suppressed in the $CaZrO_3$ materials, as the oxygen vacancy was stable in the distorted ZrO_6 symmetry. However, the protons dissolved by the direct hydrogen dissolution were stabilized near the Mn ions in the interstitial sites at the distorted MnO_6 octahedron symmetry.

The TG results of $Ca(Zr_{1-x}Mn_x)O_{3-\delta}$ (x=0.05) showed that oxygen vacancies were formed in a dry 0.8% H_2 atmosphere. The Mn K-edge XANES spectra of the dry 1% H_2 atmosphere showed that the absorption edge was between that of MnO and $LaMnO_3$. It was closer to that of MnO. Therefore, the Mn ion in $Ca(Zr_{1-x}Mn_x)O_{3-\delta}$ (x=0.05) should be between the Mn^{2+} and Mn^{3+} states. Assuming that the weight decrease in the TG measurement was caused by the formation of oxygen vacancies, the concentrations of oxygen vacancies, $[V_O^{\cdot\cdot}]$, was calculated using the following equation

$$V_O^{\cdot\cdot} = \frac{M_s}{M_O}\frac{\Delta w}{w_s} \tag{5}$$

where Δw, w_s, M_s, and M_O are the weight change, the weight of the sample, the molar weight of the sample at the stoichiometric composition, and the molar weight of oxygen, respectively. The

calculated $[V_O^{\cdot\cdot}]$ from the weight decrease was $V_O^{\cdot\cdot} = 0.026$. Assuming Ca^{2+}, Zr^{4+}, and O^{2-} states and all the Mn ions were either Mn^{2+} or Mn^{3+} states, the oxygen vacancies δ were calculated for $Ca(Zr_{1-x}Mn_x)O_{3-\delta}$ ($x=0.05$) as $\delta = 0.05$ or $\delta = 0.025$, respectively. The TG results only corresponded to $[V_O^{\cdot\cdot}]$ for Mn^{3+} state, but the XANES results suggested a further reduction than the Mn^{3+} state.

If the reduced Mn ions to Mn^{2+} and Mn^{3+} states were fully charge compensated by the oxygen vacancies, they should have caused a further decrease in the weight of the TG measurements. However, the weight decrease only corresponded to that of Mn^{3+} state. Therefore, in addition to the formation of oxygen vacancies, the redox protonation reactions of Eq.(3) and (4) should have proceeded in this material in a dry H_2 atmosphere. It was assumed that the estimated amount of oxygen vacancies $V_O^{\cdot\cdot} = 0.026$ was small compared to the actual δ.

The Mn K-edge XANES results showed no difference in the electronic state of the Mn ion between the wet and dry atmospheres. Hence, the weight increase in a wet 1% H_2 atmosphere from a dry 1% H_2 atmosphere was due to the hydration dissolution expressed by Eq. (2). Assuming that the weight changes by the evolution and dissolution of oxygen and hydrogen were negligible, the concentrations of protonic defect $[OH_O^{\cdot}]$ were twice the concentration of the dissolved water $[H_2O]$ from Eq.(2). Then the $[OH_O^{\cdot}]$ values were calculated from the TG results using the following equation

$$[OH_O^{\cdot}] = 2[H_2O] = \frac{2M_s}{M_{H_2O}} \frac{\Delta w}{w_s} \tag{6}$$

where M_{H_2O} is the molar weight of water. The calculated $[OH_O^{\cdot}]$ from the weight increase in 1% H_2 gas from a dry to a wet atmosphere was $[OH_O^{\cdot}]=0.0028$, which was small compared to the

potential amounts of oxygen vacancies in $Ca(Zr_{1-x}Mn_x)O_{3-\delta}$ (x=0.05). This is consistent with the fact that the hydration reaction was suppressed in the CZM materials.

The water dissolution was reported to be small in $CaZr_{0.9}In_{0.1}O_{3-\delta}$; it is about 1/40 of that typical proton conducting oxides $SrCe_{0.95}Yb_{0.05}O_{3-\delta}$ and $BaCe_{0.95}Yb_{0.05}O_{3-\delta}$.[26] Hence, the hydration reaction proceeds poorly in the $CaZrO_3$ materials. Okuyama $et\ al.$ reported the electrical conductivity of CZM in which the electrical conductivity was one order of magnitude higher than that of $CaZr_{0.9}In_{0.1}O_{3-\delta}$ in a H_2 atmosphere.[32] This is explained by the increased proton conductivity owing to the additional protonation via hydrogen dissolution in CZM. On the other hand, the activation energies calculated from the electrical conductivity in a H_2 atmosphere were 0.66 eV and 0.63 eV for $Ca(Zr_{1-x}Mn_x)_xO_{3-\delta}$ x=0.05 and 0.005, respectively, which were similar with those for $CaZr_{0.9}In_{0.1}O_{3-\delta}$[47] and in the DFT calculation[46,48,49] in In-doped $CaZrO_3$.

The proton diffusion mechanism in the bulk should be the same for Mn-and In-doped $CaZrO_3$ materials in spite of the different protonation mechanisms. Unlike many of typical perovskite-type proton conductors, protonation by direct dissolution of hydrogen is predominant in CZM not hydration. This is a phenomenon specific to the perovskite-type oxides. Therefore, the concentration of protonic defects could be tailored by controlling the local structure. The results in this paper experimentally showed that the structure configurations around the dopants play important roles in the stabilization of protons. To optimize the advantages of $CaZrO_3$ materials, tailoring of the local structures should improve the proton dissolution and proton conductivity.

5. CONCLUSION

The TG analysis revealed the evolution of oxygen and the dissolution of hydrogen in the H_2

atmospheres. The XAFS results showed that the valence states of the Mn ions changed from the tetra/tri-valent states in an O_2 atmosphere to the tri/di-valent states in a H_2 atmosphere. In contrast, the electronic state and local structure of the Zr ions were mostly unchanged between the O_2 and H_2 atmospheres. The average valence states of the Mn ions decreased with the increase of the H_2 activity and the Mn ion concentrations. These results support the hydrogen dissolution reaction in CZM where protons were directly dissolved to the crystal to charge compensate for the reduced Mn ions. Moreover, the MnO_6 octahedron was distorted in a H_2 atmosphere, which also depended on the H_2 activity and the Mn ion concentrations. The hydrogen dissolution reaction caused distortion of the local structure around the Mn ions, indicating the dissolution of protons near the reduced Mn ions sites. This paper experimentally showed that the structural configurations around dopants play important roles in the stabilization of protons in perovskite-type CZM materials.

SUPPORTING INFORMATION

Additional experimental information of XRD analysis, structure parameters, XAFS measurements and simulation of EXAFS spectrum.

AUTHORS INFORMATION

Corresponding Author

E-mail: ooishi.masatsugu@tokushima-u.ac.jp

ORCID

Masatsugu Oishi: 0000-0002-4561-1038

Takashi Nakamura: 0000-0001-5461-9958

Yuji Okuyama: 0000-0003-0891-1258

Notes

There are no conflicts to declare.

ACKNOWLEDGEMENTS

REFERENCES

(1) Minh N.Q. Ceramic fuel cells. *J. Am. Ceram. Soc.* **1993**, *76*, 563-588.

(2) Singhal, S; Kendall K. Eds., High-temperature solid oxide fuel cells: fundamentals, design and applications (Elsevier , NY , 2003).

(3) Wachsman E.; Ishiraha T.; Kilner J. Low-temperature solid-oxide fuel cells. *MRS bulletin* **2014**, *39*, 773-797.

(4) Duan C.; Kee R.; Zhu H.; Sullivan N.; Zhu L.; Bian L.; Jennings D.; O'Hayre R.; Highly efficient reversible protonic ceramic electrochemical cells for power generation and fuel production. *Nat. Energy* **2019**, *230*, 230–240.

(5) Takahashi T.; Iwahara H. Solid state ionics, protonic conduction in perovskite type oxide solid-

solutions. *Rev. Chim. Miner.* **1980**, *17*, 243–253.

(6) Kreuer K.-D. Proton-conduction oxides. *Annu. Rev. Mater. Res.* **2003**, *33*, 333-359.

(7) Kreuer, K.-D. Proton conductivity: Materials and applications. *Chem. Mater.* **1996**, *8*, 610−641.

(8) Iwahara H. Technological challenges in the application of proton conducting ceramics. *Solid State Ionics* **1995**, *77*, 289-298.

(9) Norby, T. Solid-state protonic conductors: principles, properties, progress and prospects. *Solid State Ionics* **1999**, *125*, 1−11.

(10) Okuyama Y.; Okuyama K.; Mizutani Y.; Sakai T.; Lee Y. S.; H. Matsumoto H. Proton transport properties of $La_{0.9}Sr_{0.1}Yb_{0.8}In_{0.2}O_{3-d}$ and its application to proton ceramic fuel cell. *Int. J. Hydrogen Energy* **2014**, *39*, 20829–20836.

(11) Sata N; Hiramoto K.; Ishigame M.; Hosoya S.; Niimura N.; Shin S. Site identification of proton in $SrTiO_3$: Mechanism for larger protonic conduction. *Phys, Rev. B*, **1996**, *54*, 795-799.

(12) Kreuer K.-D., On solids with liquidlike properties and the challenge to develop new proton-conducting separater material for intermediate-temperature fuel cell. *Chem. Phys. Chem.* **2002**, *3*, 771-775.

(13) Duan C.; Kee R.J.; Zhu H.; Karakaya C.; Chen Y.; Ricote S.; Jarry A.; Crumlin E.J.; Hook D.; Braun R.;, Sullivan N.P.; O'Hayre R. Highly durable, coking and sulfur tolerant, fuel-flexible protonic ceramic fuel cells. *Nature* **2018**, *557*, 217-222.

(14) Ito N.; Iijima M.; Kimura K.; Iguchi S. New intermediate temperature fuel cell with ultra-thin proton conductor electrolyte. *J. Power Sources* **2005**, *152*, 200–203.

(15) Ito N.; Aoyama S.; Masui T.; Matsumoto S.; Matsumoto H.; and Ishihara T. Electrochemical analysis of hydrogen membrane fuel cells. *J. Power Sources* **2008**, *185*, 922–926.

(16) Duan C.; Tong J.; Shang M.; Nikodemski S.; Sanders M.;, Ricote S.; Almansoori A.; O'Hyre

R. Readily processed protonic ceramic fuel cells with high performance at low temperatures. *Science* **2015**, *349*, 1321–1326.

(17) Oishi M.; Akoshima S.; Yashiro K.; Sato K.; Mizusaki J.; Kawada T. Defect structure analysis of B-site doped perovskite-type proton conducting oxide $BaCeO_3$: Part 2: The electrical conductivity and diffusion coefficient of $BaCe_{0.9}Y_{0.1}O_3$. *Solid State Ionics* **2008**, *179*, 2240-2247.

(18) Yashiro K.; Akoshima S.; Kudo T.; Oishi M.; Matsumoto H.; Sato K.; Kawada T.; Mizusaki J. Electrical conductivity and chemical diffusion in perovskite-type proton conductors in H_2/H_2O gas mixtures. *Solid State Ionics* **2011**, *192*, 76-82, 2011.

(19) Kreuer K.-D. Aspects of the formation and mobility of protonic charge carriers and the stability of perovskite-type oxides. *Solid State Ionics* **1999**, *125 (1-4)*, 285–302.

(20) Yamazaki, Y.; Blanc, F.; Okuyama, Y.; Buannic, L.; Lucio-Vega, J. C.; Grey, C. P.; Haile, S. M. Proton trapping in yttrium-doped barium zirconate. *Nat. Mater.* **2013**, *12*, 647−651.

(21) Imashuku, S.; Uda, T.; Nose, Y.; Taniguchi, G.; Ito, Y.; Awakura, Y. Dependence of dopant cations on microstructure and proton conductivity of barium zirconate. *J. Electrochem. Soc.* **2009**, *156*, B1-B8.

(22) Ryu, K. H.; Haile, S. M. Chemical stability and proton conductivity of doped $BaCeO_3$-$BaZrO_3$ Solid Solutions. *Solid State Ionics* **1999**, *125*, 355−367.

(23) Yajima, T.; Koide, K.; Takai, H.; Fukatsu, N.; Iwahara, H. , Application of hydrogen sensor using proton conductive ceramics as a solid electrolyte to aluminum casting industries, *Solid State Ionics* **1995**, *79*, 333-337.

(24) Fukatsu, N.; Kurita, N.; Koide, K.; Ohashi, T. ,Hydrogen sensor for molten metals usable up to 1500 K, *Solid State Ionics* **1998**, *115*, 219-227.

(25) Islam M. S,; Davies, R. A.; and Gale J. D, Proton migration and defect interactions in the

CaZrO$_3$ orthorhombic perovskite: A quantum mechanical study, *Chem. Mater.* **2001**, *13*, 2049-2055.

(26) Hibino T.; Mizutani K.; Yajima T.; Iwahara H, Evaluation of proton conductivity in SrCeO$_3$, BaCeO$_3$, CaZrO$_3$ and SrZrO$_3$ by temperature programmed desorption method. *Solid State Ionics* **1992**, *57*, 303-306.

(27) Yajima T.; Kazeoka H.; Yogo T.; Iwahara H. Proton conduction in sintered oxides based on CaZrO$_3$. *Solid State Ionics* **1991**, *47*, 271-275.

(28) Kröger F.A. The chemistry of imperfect crystals. North-Holland, Amsterdam, 1974.

(29) Kreuer K.-D.; Adams St.; Münch W.; Fuchs A.; Klock U.; Maier J. Proton conducting alkane earth zirconates and titanates for high drain electrochemical applications. *Solid State Ionics* **2001**,*145*, 295-306.

(30) Takahashi H.; Yashima I.; Amezawa K.; Eguchi K.; Matsumoto H.; Takamura H.; Yamaguchi S. First-principles calculations for the energetics of the hydration reaction of acceptor-doped BaZrO$_3$. *Chem. Mater.* **2017**, *29*, 1518-1526.

(31) Stokes S. J.; Islam M. S., Defect chemistry and proton-dopant association in BaZrO$_3$ and BaPrO$_3$, *J. Mater. Chem.*, **2010**, *20*, 6258–6264.

(32) Okuyama Y.; Nagamine S.; Nakajima A.; Sakai G.; Matsunaga N.; Takahashi F.; Kimata K.; Oshima T.; Tsuneyoshi K. Proton-conducting oxide with redox protonation and its application to a hydrogen sensor with a selfstandard electrode. *RSC Adv.* **2016**, *6*, 34019-34026.

(33) Oishi M.; Akoshima S.; Yashiro K.; Sato K.; Mizusaki J.; Kawada T. Defect structure analysis of B-site doped perovskite-type proton conducting oxide BaCeO$_3$ Part 1: The defect concentration of BaCe$_{0.9}$M$_{0.1}$O$_{3-\delta}$ (M = Y and Yb). *Solid State Ionics* **2009**, *180*, 127-131.

(34) Oishi M.; Akoshima S.; Yashiro K.; Sato K.; Kawada T.; Mizusaki J. Defect structure analysis

of proton-oxide ion mixed conductor $BaCe_{0.9}Nd_{0.1}O_{3-\delta}$. *Solid State Ionics* **2010**, *181*, 1336-1343.

(35) Müller R.; Günthard Hs. H. Spectroscopic study of the reduction of nickel and cobalt ion in sapphire. *J. Chem. Phys.* **1966**, *44*, 365–373.

(36) Eigenmann K.; Günthard Hs. H. Hydrogen incorporation in doped *a*-Al_2O_3 by high temperature redox reactions. *Chem. Phys. Lett.* **1971**, *12*, 12–15.

(37) Balmer P.; Blum H.; Forster M.; Schweiger A.; Günthard Hs. H. Co^{z+} *a* -Al_2O_3: cobalt and proton ENDOR, infrared and optical spectra, the nature of charge compensator and the structure of the defect (Co^{2+}, H^+): a-Al_2O_3. *J. Phys. C: Solid State Phys.* **1980**, *13*, 517–534.

(38) Matsumoto H.; Sakai T.; Kawasaki Y.; Sato Y.; Ishihara T. Abstract of SSPC-15, **2010**, 24.

(39) Uruga T.; Tanida H.; Yoneda Y.; Takeshita K.; Emura S.; Takahashi M.; Harada M.; Nishihata Y.;, Kubozono Y.; Tanaka T.; Yamamoto T.; Maeda H.; Kamishima O.; Takabayashi Y.; Nakata Y.; Kimura H.; Goto S.; Ishikawa T.;, The XAFS beamline BL01B1 at SPring-8, *J. Synchrotron Rad.*, **1999**, *6*, 143-145.

(40) Ravel B.; Newville M. ATHENA, ARTEMIS, HEPHAESTUS: Data Analysis for X-Ray Absorption Spectroscopy Using IFEFFIT. *J. Synchrotron Radiat* **2005**, *12*, 537–541.

(41) Izumi F.; Momma K.; Three-dimensional visualization in powder diffraction. *Solid State Phenom.* **2007**, *130*, 15–20.

(42) Levin I.; Amos T. G.; Bell S. M.; Farber L.; Vanderah T. A.; Roth R. S.; Toby B. H. Phase equilibria, crystal structures, and dielectric anomaly in the $BaZrO_3$–$CaZrO_3$ system. *J. Solid State Chem.* **2003**, *175*, 170–181.

(43) Shannon R.D. Revised effective ionic radii and systematic studies of interatomic distances in halides and chalcogenides. *Acta Crystallogr., Sect. A: Cryst. Phys., Diffr.,Theor. Gen. Crystallogr.* **1976**, *32*, 751–767.

(44) Sundell, P. G.; Björketun M. E.; Wahnström G, Thermodynamics of doping and vacancy formation in BaZrO$_3$ perovskite oxide from density functional calculations, *Phys. Rev. B* **2006**, *73*, 104112 1-10.

(45) Daviesa, R. A.; Islam M. S.; Gale J.D., Dopant and proton incorporation in perovskite-type zirconates, *Solid State Ionics* **1999**, *126*, 323–335.

(46) Islam M. S.; Davies R. A.; Gale J. D. Hop, skip or jump? Proton transport in the CaZrO$_3$ perovskite oxide. *Chem. Commun.* **2001**, 661-662.

(47) Kurita N.; Fukatsu N; Ito K.; Ohashi T. Protonic conduction domain of indium-doped calcium zirconate. *J. Electrochem. Soc.*, **1995**, *142*, 1552–1559.

(48) Bilić A.; Gale J. D. Proton mobility in the In-doped CaZrO$_3$ perovskite oxide. *Chem. Mater.* **2007**, *19*, 2842-2851.

(49) Bilić A; Gale J. D. Simulation of proton diffusion in In-doped CaZrO$_3$. *Solid State Ionics* **2008**, *179*, 871-874.

Table 1. Lattice parameters of $Ca(Zr_{1-x}Mn_x)O_3$ (x=0.005, 0.015, 0.05) in the O_2 atmospheres and H_2 atmospheres in the space group of *Pnma*.

$CaZr_{1-x}Mn_xO_{3-\delta}$							
x	Annealing conditions	a (Å)	b (Å)	c (Å)	V (Å³)	R_{wp} (%)	S
0.005	98.1%O_2-1.9%H_2O	5.591	8.017	5.762	258.270	8.58	1.158
	1%O_2-1.9%H_2O-Ar	5.590	8.015	5.762	258.160	8.03	1.112
	1%H_2-1.9%H_2O-Ar	5.590	8.017	5.761	258.180	8.06	1.150
	98.1%H_2-1.9%H_2O	5.592	8.017	5.756	258.048	8.43	1.210
0.015	98.1%O_2-1.9%H_2O	5.592	8.014	5.755	257.906	7.93	1.057
	1%O_2-1.9%H_2O-Ar	5.591	8.014	5.755	257.860	7.73	1.065
	1%H_2-1.9%H_2O-Ar	5.592	8.017	5.756	258.048	7.95	1.058
	10%H_2-1.9%H_2O-Ar	5.592	8.018	5.757	258.125	7.40	1.034
	98.1%H_2-1.9%H_2O	5.592	8.018	5.758	258.170	7.52	1.018
0.05	98.1%O_2-1.9%H_2O	5.590	8.006	5.742	256.947	7.93	1.031
	1%O_2-1.9%H_2O-Ar	5.591	8.007	5.743	257.096	8.08	1.026
	1%H_2-1.9%H_2O-Ar	5.593	8.013	5.747	257.548	7.99	1.101
	10%H_2-1.9%H_2O-Ar	5.595	8.016	5.748	257.772	9.56	1.193
	98.1%H_2-1.9%H_2O	5.594	8.014	5.748	257.679	8.15	1.072

Table 2. Fitting results of the first coordination shells in the q space of the reverse FT spectra of Mn K-edge obtained between radical range of 1 and 2 Å . Numbers in bracket indicate the standard deviation.

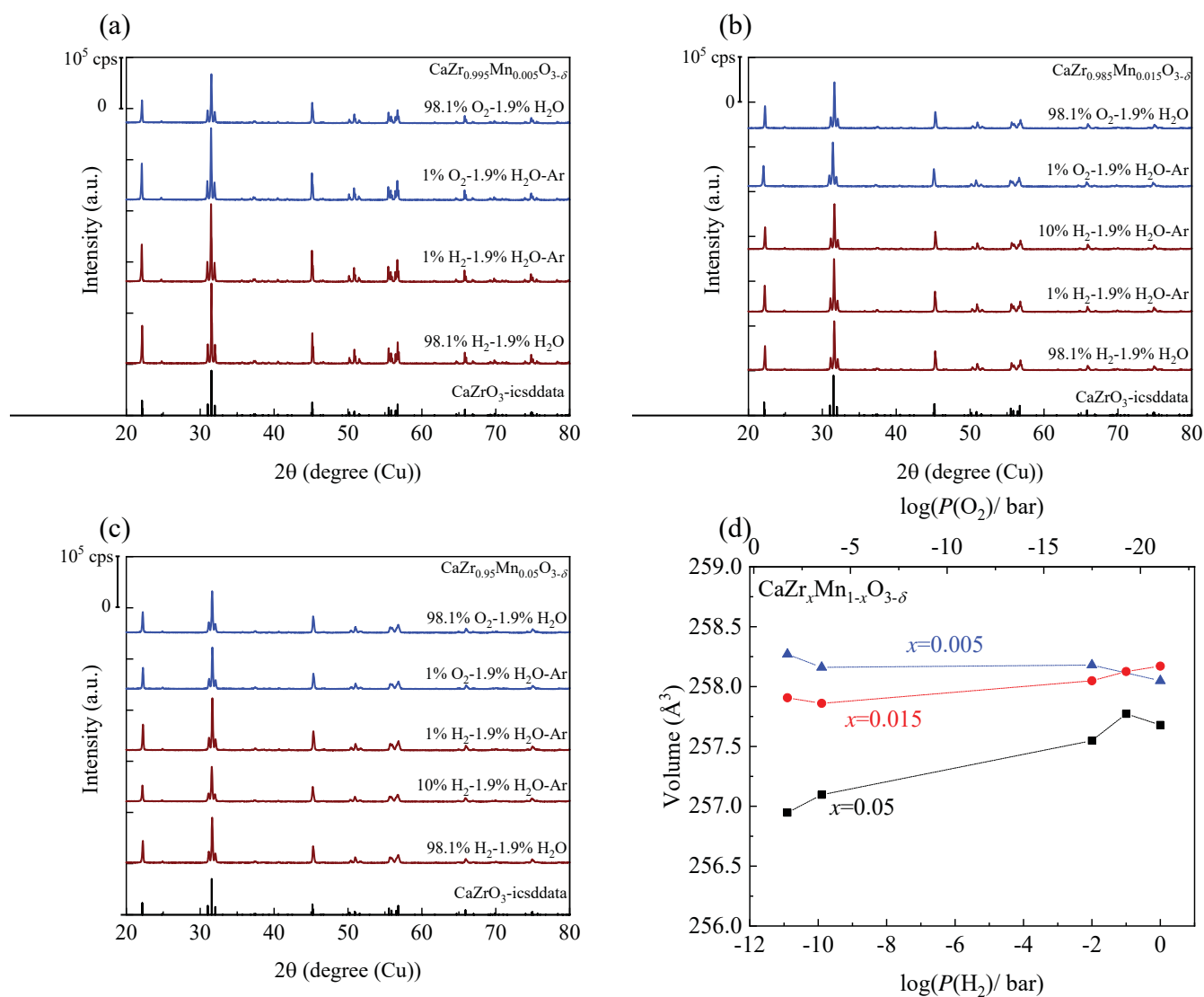| $CaZr_{1-x}Mn_xO_{3-\delta}$				Mn-O		
x	Annealing conditions	N	r (Å)	σ^2 (Å^2)	ΔE_0 (eV)	R (%)
0.005	98.1%O_2-1.9%H_2O	4.8 (0.42)	1.96 (0.005)	0.0021 (0.0006)	-0.68 (1.27)	0.25
	1%O_2-1.9%H_2O-Ar	5.5 (0.80)	1.95 (0.009)	0.0037 (0.0011)	-2.48 (2.15)	0.69
	1%H_2-1.9%H_2O-Ar	4.3 (0.63)	1.96 (0.009)	0.0029 (0.0011)	-3.58 (2.13)	0.69
	98.1%H_2-1.9%H_2O	3.4 (0.16)	1.96 (0.000)	0.0019 (0.0003)	-3.32 (0.70)	0.06
0.015	98.1%O_2-1.9%H_2O	4.8 (0.53)	1.94 (0.007)	0.0028 (0.0008)	-3.59 (1.65)	0.38
	1%O_2-1.9%H_2O-Ar	4.71 (0.46)	1.95 (0.006)	0.0029 (0.0007)	-3.22 (1.44)	0.29
	1%H_2-1.9%H_2O-Ar	3.9 (0.50)	1.96 (0.008)	0.0034 (0.0010)	-5.11 (1.88)	0.49
	10%H_2-1.9%H_2O-Ar	3.4 (0.57)	1.96 (0.010)	0.0023 (0.0012)	-7.14 (2.55)	0.82
	98.1%H_2-1.9%H_2O	4.1 (0.76)	1.97 (0.012)	0.0050 (0.0015)	-4.45 (2.71)	1.07
0.05	98.1%O_2-1.9%H_2O	5.1 (0.62)	1.93 (0.008)	0.0038 (0.0008)	-0.93 (1.88)	1.05
	1%O_2-1.9%H_2O-Ar	5.2 (0.56)	1.93 (0.007)	0.0039 (0.0007)	-1.76 (1.67)	0.81

Figure 1. XRD profiles of $Ca(Zr_{1-x}Mn_x)O_{3-\delta}$ $x=$ (a) 0.005, (b) 0.015 and (c) 0.05 in the O_2 atmospheres and H_2 atmospheres. (d) The volumes calculated from the lattice parameters obtained from the Rietveld analysis.
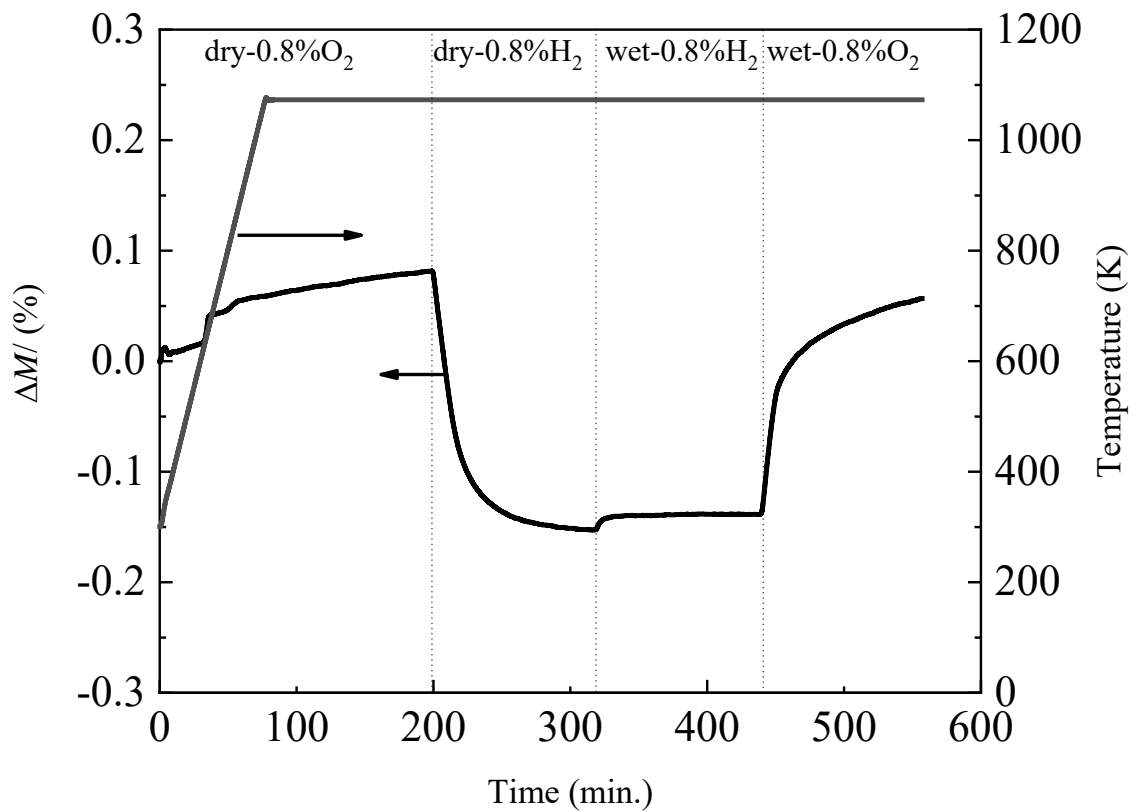
Figure 2. The weight change of $CaZr_{0.95}Mn_{0.05}O_{3-\delta}$ in 0.8 %O_2-99.2 %Ar gas and 0.8 %H_2-99.2 %Ar gas in dry and wet ($P(H_2O)$= 0.019 bar) conditions.
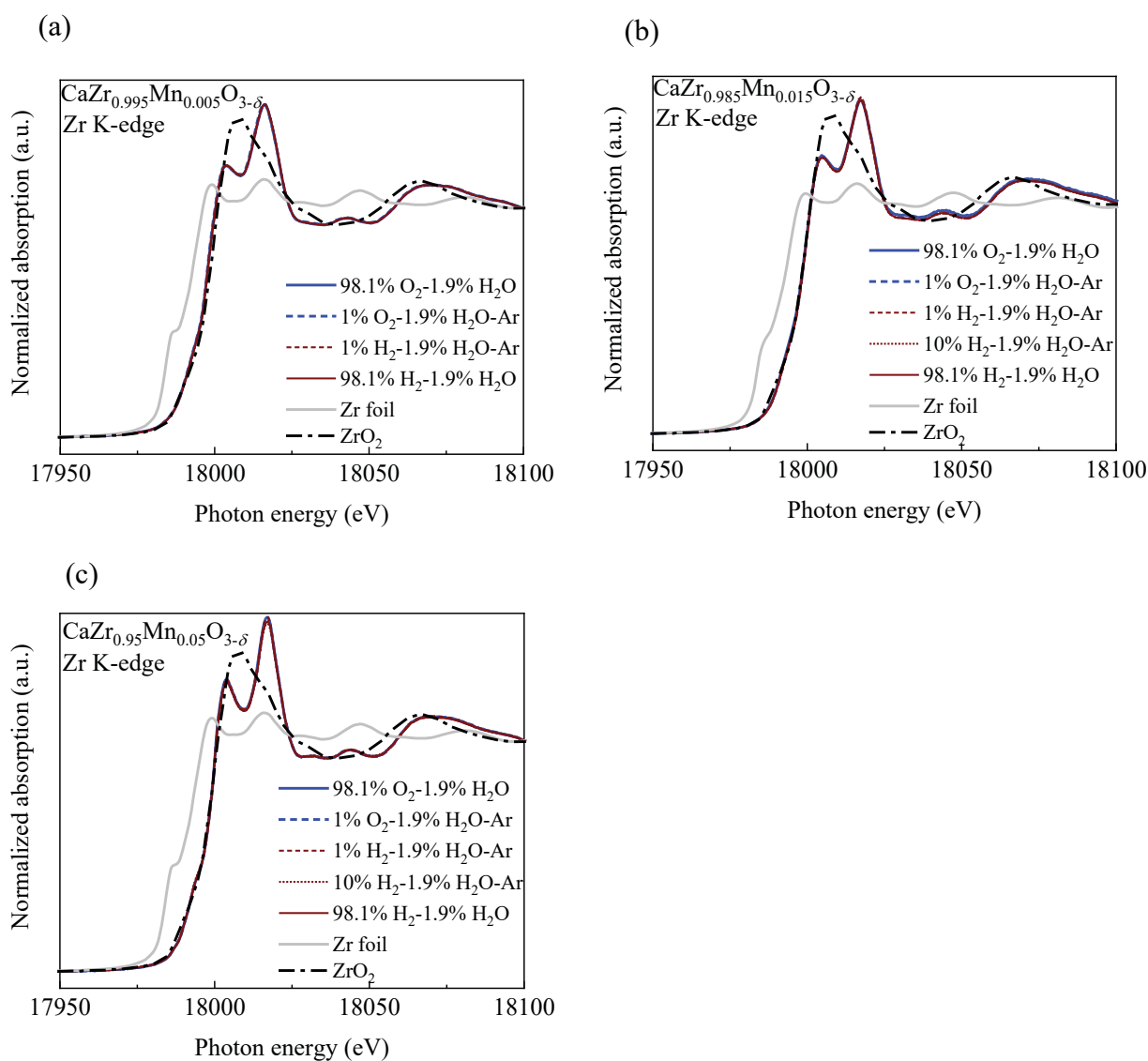
Figure 3. Zr K-edge XANES spectra of $Ca(Zr_{1-x}Mn_x)O_{3-\delta}$ $x=$ (a) 0.005, (b) 0.015 and (c) 0.05 in O_2 atmospheres and H_2 atmospheres. Included are the spectra for Zr foil and ZrO_2 as reference spectra for Zr^0 and Zr^{4+} ions, respectively.
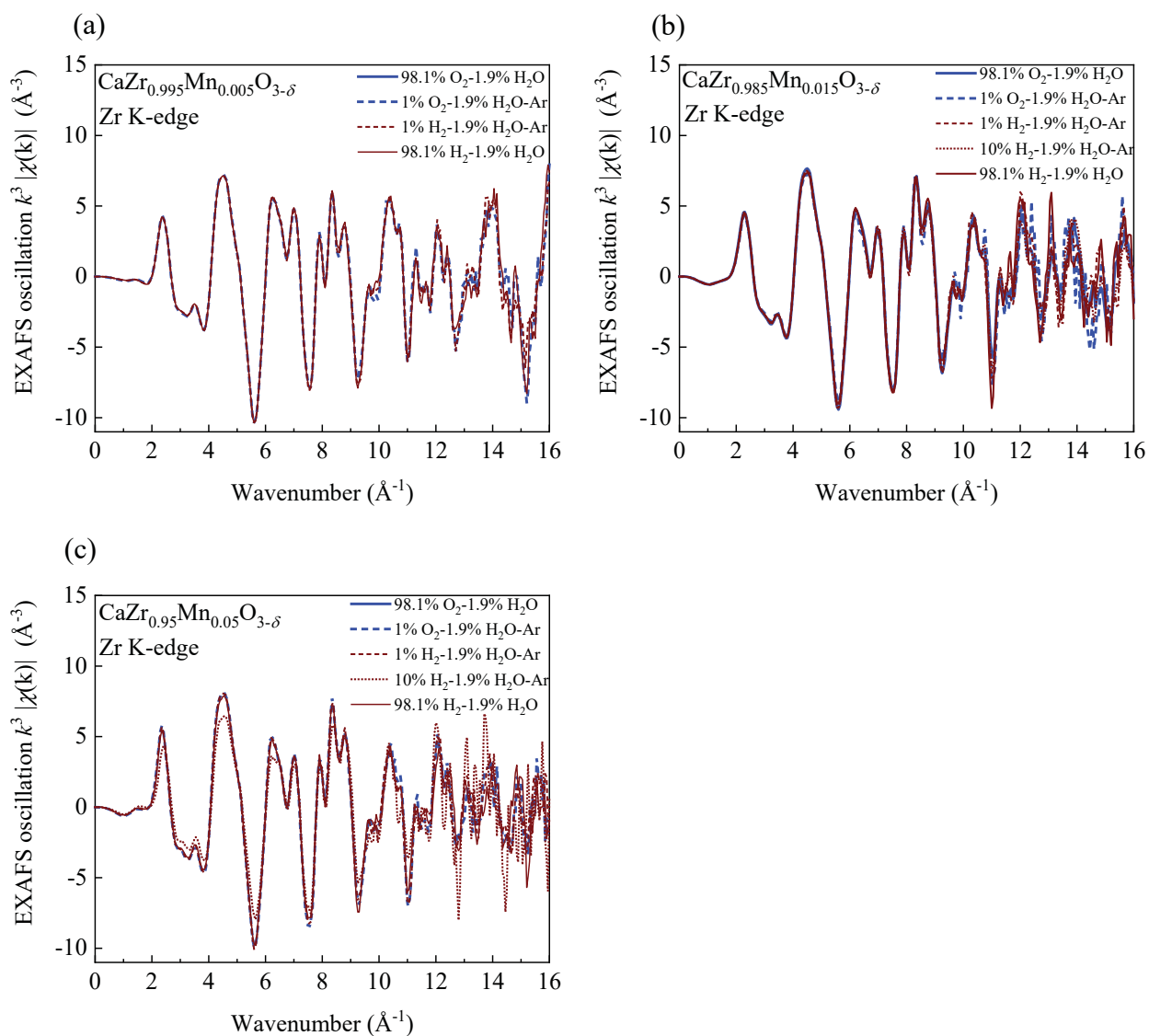
Figure 4. Zr K-edge EXAFS oscillation of $Ca(Zr_{1-x}Mn_x)O_{3-\delta}$ $x=$ (a) 0.005, (b) 0.015 and (c) 0.05 in the O_2 atmospheres and H_2 atmospheres.
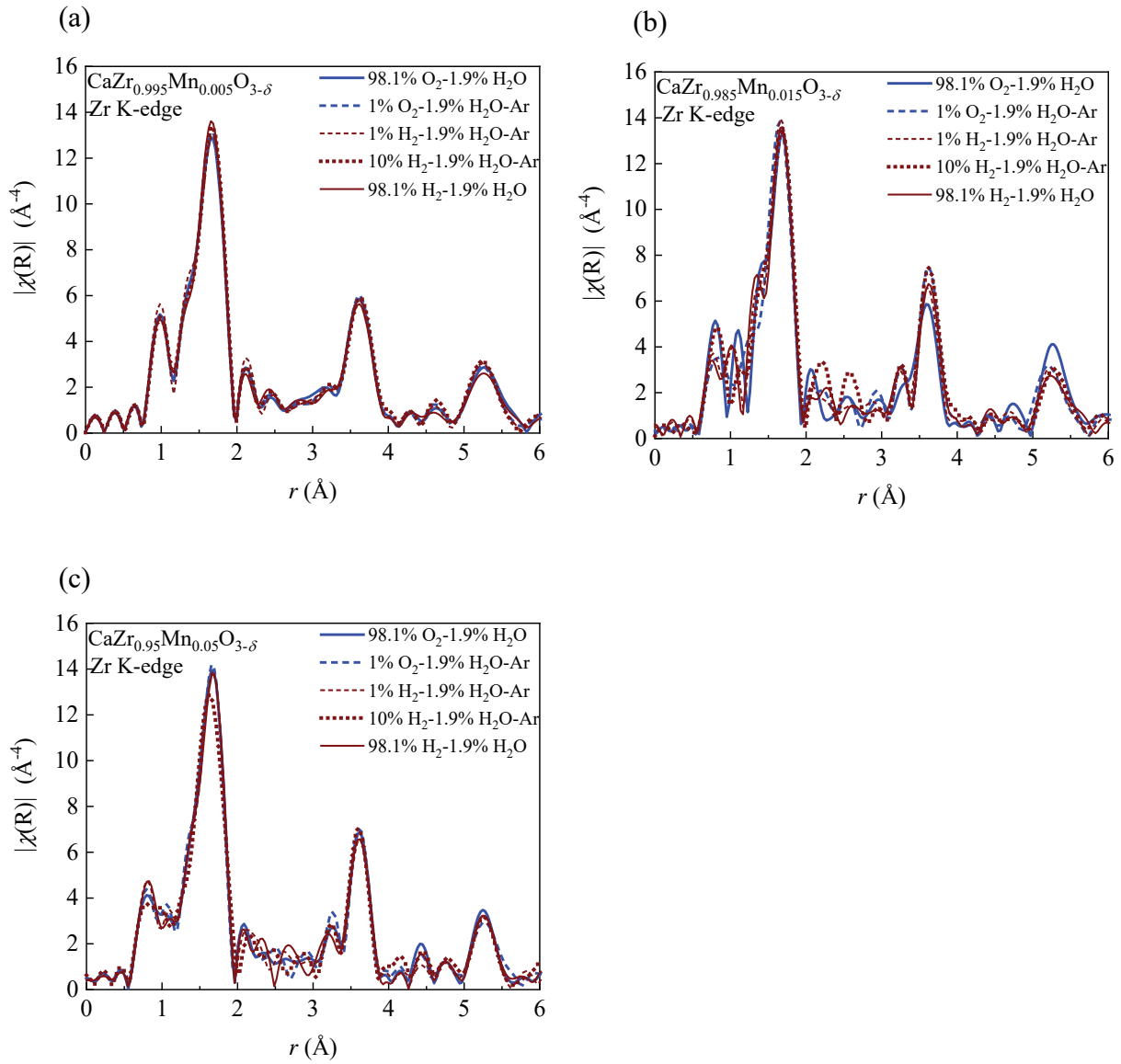
Figure 5. The amplitudes of Fourier transforms obtained from EXAFS oscillations of CaZr$_{1-x}$Mn$_x$O$_{3-\delta}$ $x=$ (a) 0.005, (b) 0.015 and (c) 0.05 in the O$_2$ atmospheres and H$_2$ atmospheres.
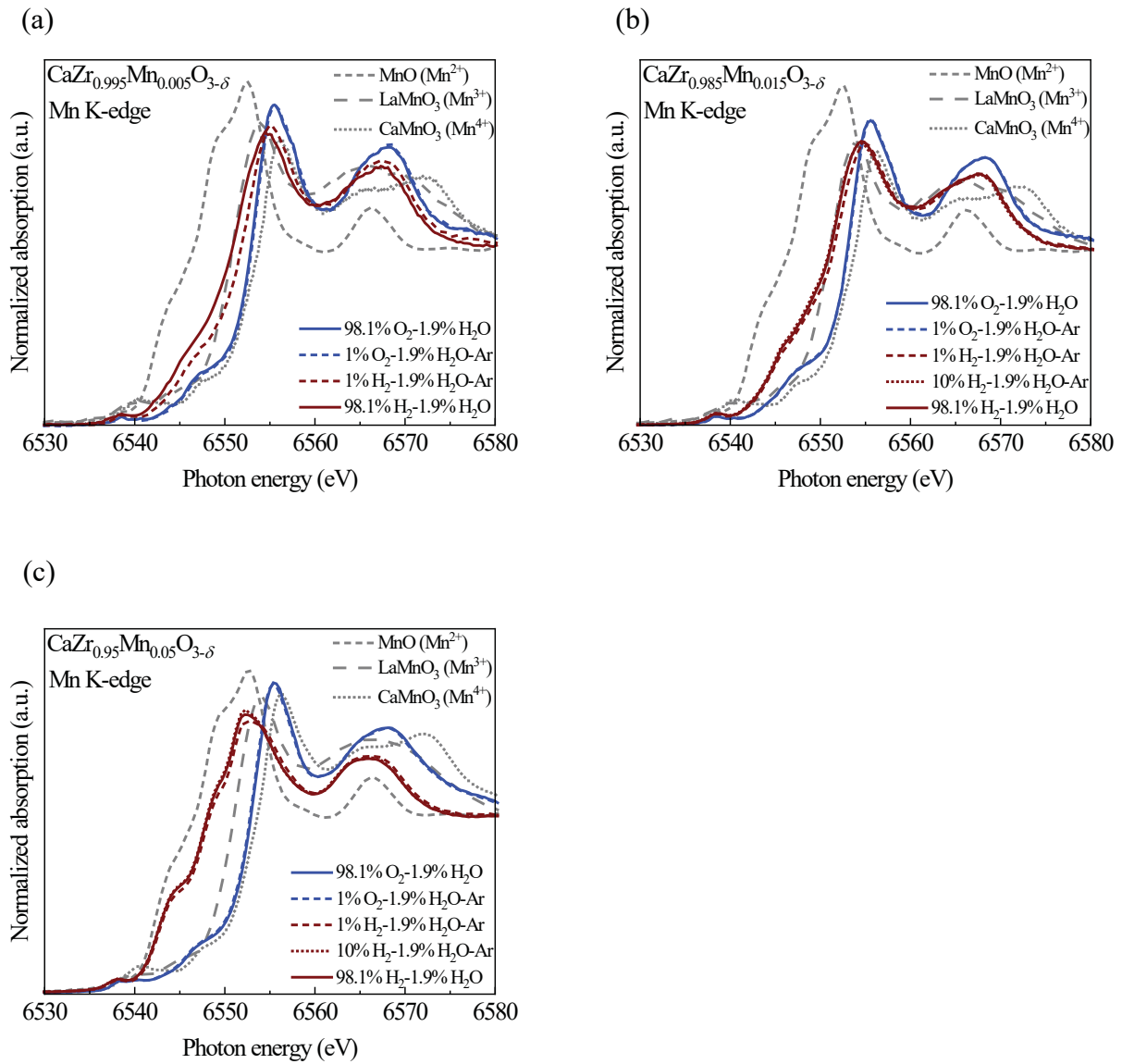
Figure 6. Mn K-edge XANES spectra of $CaZr_{1-x}Mn_xO_{3-\delta}$ $x=$ (a) 0.005, (b) 0.015 and (c) 0.05 in the O_2 atmospheres and H_2 atmospheres.

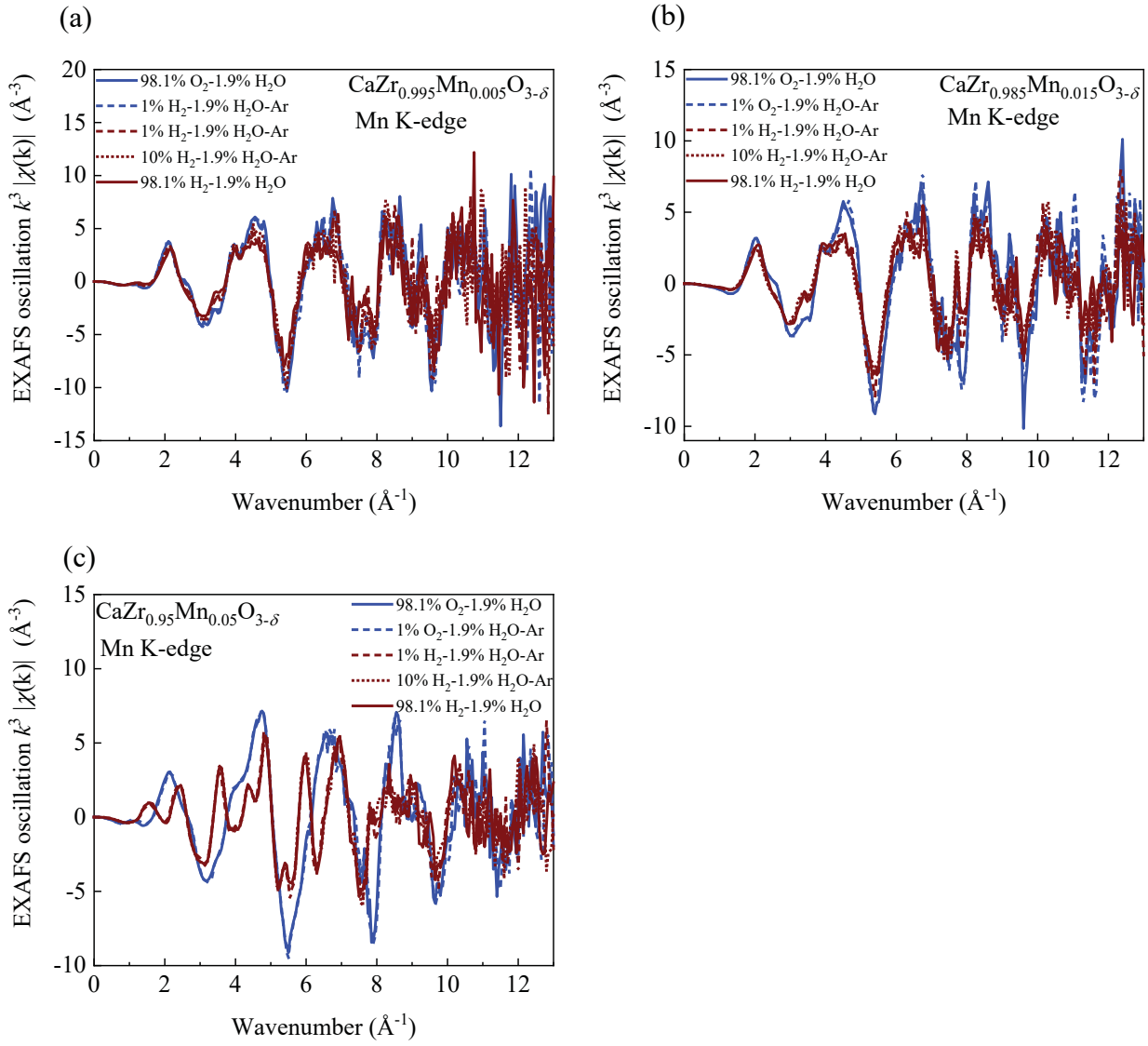(a) CaZr$_{0.995}$Mn$_{0.005}$O$_{3-\delta}$ Mn K-edge

Legend:
- 98.1% O$_2$-1.9% H$_2$O
- 1% H$_2$-1.9% H$_2$O-Ar
- 1% H$_2$-1.9% H$_2$O-Ar
- 10% H$_2$-1.9% H$_2$O-Ar
- 98.1% H$_2$-1.9% H$_2$O

(b) CaZr$_{0.985}$Mn$_{0.015}$O$_{3-\delta}$ Mn K-edge

Legend:
- 98.1% O$_2$-1.9% H$_2$O
- 1% O$_2$-1.9% H$_2$O-Ar
- 1% H$_2$-1.9% H$_2$O-Ar
- 10% H$_2$-1.9% H$_2$O-Ar
- 98.1% H$_2$-1.9% H$_2$O

(c) CaZr$_{0.95}$Mn$_{0.05}$O$_{3-\delta}$ Mn K-edge

Legend:
- 98.1% O$_2$-1.9% H$_2$O
- 1% O$_2$-1.9% H$_2$O-Ar
- 1% H$_2$-1.9% H$_2$O-Ar
- 10% H$_2$-1.9% H$_2$O-Ar
- 98.1% H$_2$-1.9% H$_2$O

Figure 7. Mn K-edge EXAFS oscillation of CaZr$_{1-x}$Mn$_x$O$_{3-\delta}$ $x=$ (a) 0.005, (b) 0.015 and (c) 0.05 in the O$_2$ atmospheres and H$_2$ atmospheres.
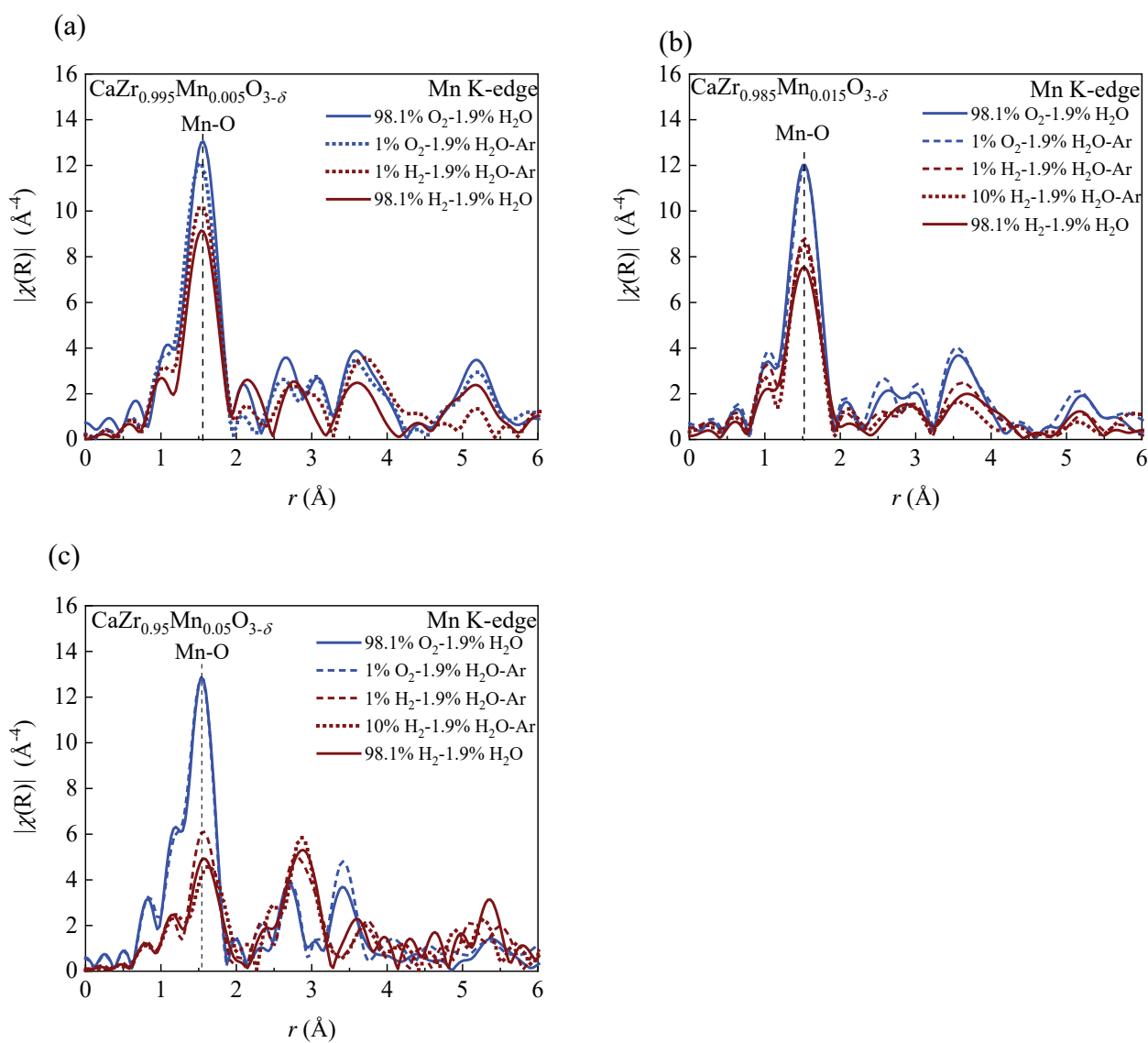
Figure 8. The amplitudes of Fourier transforms obtained from EXAFS oscillations of $CaZr_{1-x}Mn_xO_{3-\delta}$ $x=$ (a) 0.005, (b) 0.015 and (c) 0.05 in the O_2 atmospheres and H_2 atmospheres.
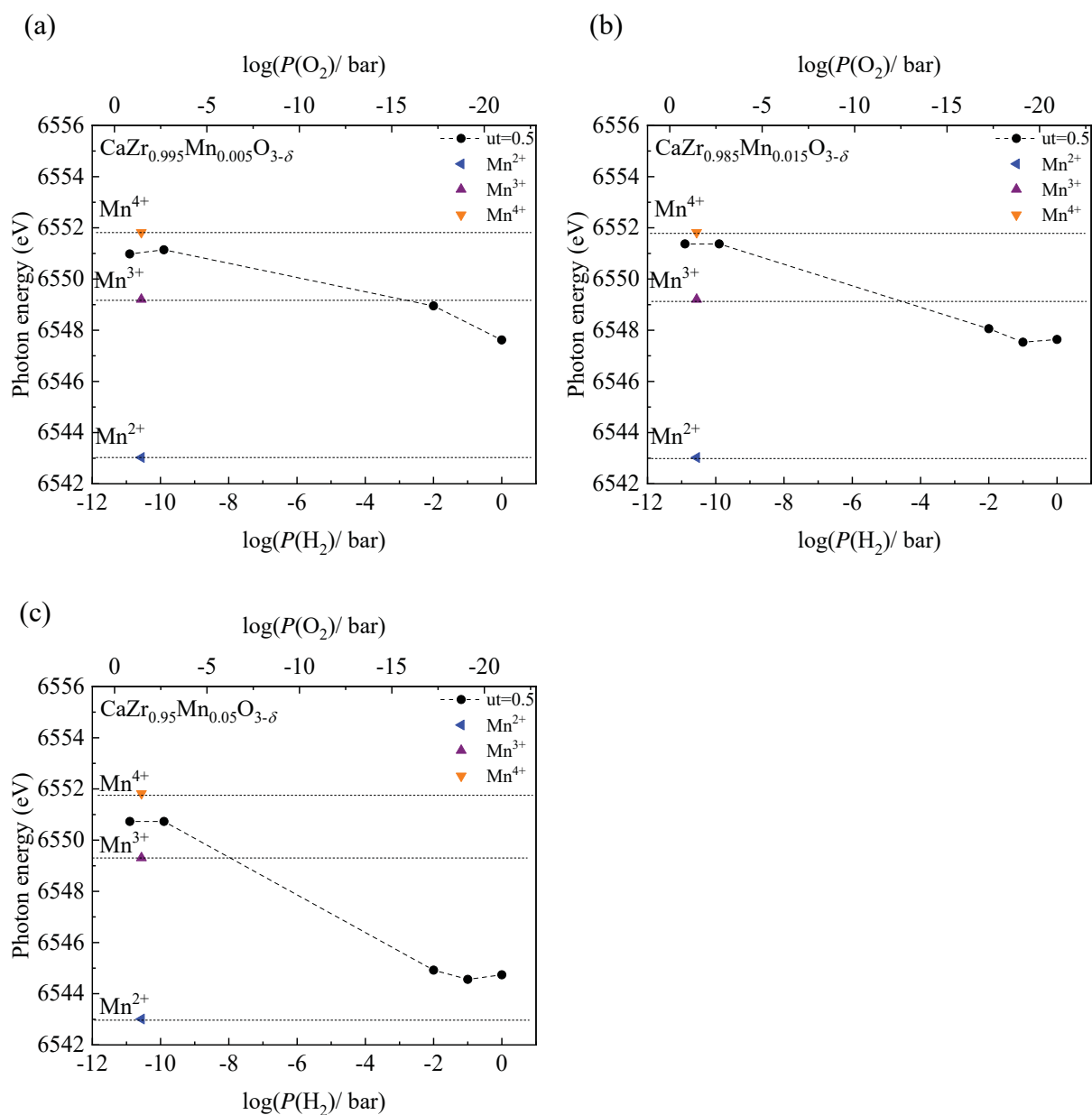
Figure 9. The Mn K-edge energy at the absorbance of 0.5 for $CaZr_{1-x}Mn_xO_{3-\delta}$ $x=$ (a) 0.005, (b) 0.015 and (c) 0.05 as a a function of $P(H_2)$ and $P(O_2)$. Its energy of Mn^{2+}, Mn^{3+} and Mn^{4+} states at $P(O_2)=0.21$ bar is those for MnO, $LaMnO_3$, and $CaMnO_3$, respectively.
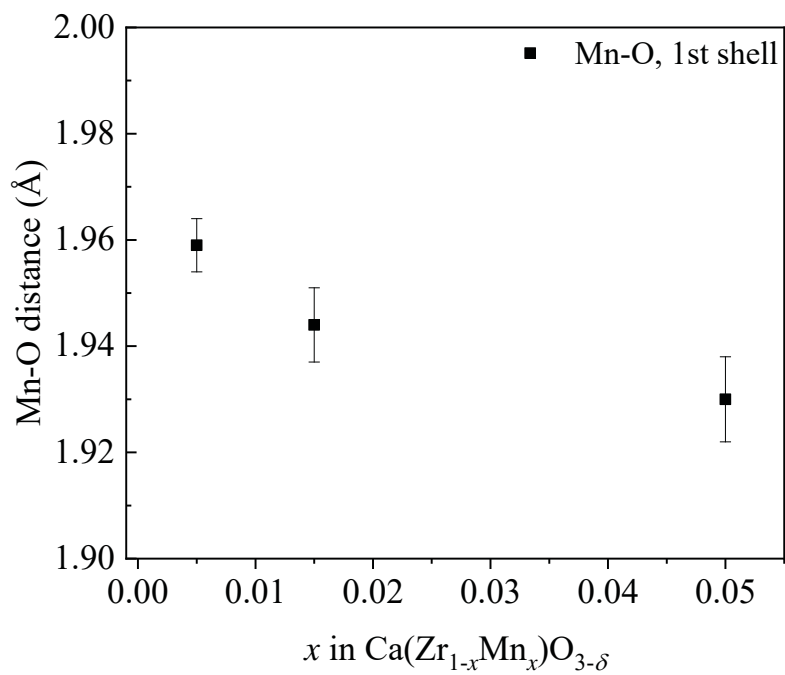
Figure 10. Comparison of the Mn-O bond length for $CaZr_{1-x}Mn_xO_{3-\delta}$ x= 0.05, 0.015 and 0.005 annealed in the 98.1%O_2 -1.9%H_2O atmosphere.